Design and Analysis of a Higher Order Power Filter for Grid-Connected Renewable Energy Systems

Arash Anzalchi, *Student Member, IEEE,* Masood Moghaddami, *Student Member, IEEE,*
Amir Moghadasi, *Member, IEEE,* Maneli Malek Pour, *Student Member, IEEE* and Arif Sarwat, *Member, IEEE*

***Abstract*—Harmonic compensation is regularly implemented for a grid-tied inverter to reduce the influence of the grid current and voltage harmonics. In this study, the *L(LCL)*$_2$ filter, which is a high order power filter for single-phase grid-tied voltage-source inverters (VSI), is designed and analyzed. In order to attenuate the high-frequency harmonics, additional resonant branch at the double of the switching frequency is added to the *LLCL* filter. The total inductance of this filter is almost less than the *LLCL* filter with the amount of the grid side inductor. A comparative study on filter parameter design, size estimation, efficiency, stability, and dc-link dynamics in bi-directional power flow applications between the *LLCL* filter and the proposed *L(LCL)*$_2$ filter have been conducted. The assessment of these studies are presented through both experimental hardware implementation and Matlab/Simulink-based simulation on a 700 W, 120V / 60 Hz single-phase grid-tied inverter. It is concluded that, compared to the *LLCL* filter, the *L(LCL)*$_2$ filter not only has less voltage drop and total component size but also has better performance on reducing high order current harmonics. Additionally, the *L(LCL)*$_2$ filter has a smaller size, less losses, stable closed loop control system, and compared to traditional *LLCL* filter, it does not add any control difficulty to the system.**

***Index Terms*—current harmonics; *LCL*-filter; *LLCL* filter; *L(LCL)*$_2$ filter; Power quality; switching-frequency; voltage-source inverter (VSI).**

I. Introduction

RENEWABLE energy sources and distributed generation (DG) resources are mostly connected to the power grid through a grid-connected inverter [1]. In order to limit the excessive current harmonics, which are mostly produced by sine pulse width modulation (PWM), a low-pass power filter is usually put in between a voltage-source inverter (VSI) and the grid [2], [3]. The use of the PWM system necessitates an output filter to limit the grid-injected current harmonics, in order to satisfy the *IEEE 1547.2-2008* and *IEEE 519-2014* standards. *L*-filters are typically used but they have the drawbacks of slow dynamic response and big inductor value [4], [5]. The first-order *L* filter can meet the standards for the grid interconnection with notably smaller size and cost compared to an *LCL* filter, primarily for applications in several kilowatts [6]–[8].

For industrial uses, the cost of the components is a vital aspect of selecting the power filter for the grid-tied inverter. Owing to the growing cost of copper, various methods have been implemented to cut down the price of the power filter. One helpful way is to increase the switching frequency of the inverter where the method, surely, depends on the device proficiency and cost.

Nowadays, most power electronic designs are limited by thermal constraints. Power dissipation and surface area have a major influence on temperature increase. The volume and size of the component are two measures that the surface area of the object is directly linked with. The use the total power loss of the *LCL* filter as the optimization factor in the design was introduced in [9]. The objective of the algorithm was to reduce the size, weight, and absolutely the cost of the *LCL* filter.

Special topologies and control configurations are other measures which have motivated scholars. [10] introduced a three-level neutral point clamped (NPC) converter as a high power renewable energy grid interface, trying to achieve higher switching frequency and better efficiency. An *LLCL* topology with two resonant circuits between the ripple inductor and the grid-side inductor i to suppress the two dominant harmonic currents around the switching frequency and the double of the switching frequency.

The conducted Electromagnetic Interference (EMI) issues for the high-order power-filter-based single-phase full-bridge grid-tied inverter by means of the unipolar modulation in discontinuous mode was considered in [11]. In order to minimize the additional reactive power as well as to achieve a small value of the capacitor, a differential mode EMI suppressor for the *LLCL* filter based system was proposed in [12]. To decrease the overall inductance value, without increasing the capacitive reactive power, the modified LCL filter topology by using an extra parallel LC resonant circuit was suggested in [13]. A capacitor-current-feedback active damping by means of reduced computation delay was proposed in [14]. By using this method, the virtual impedance functions more similar to a resistor in a wider frequency range, and the unstable poles of the open loop are eliminated; consequently, great robustness against the grid impedance deviation is attained. The magnetic integration of the LCL filter in grid-connected inverters was investigated in [15]. By placing the windings accurately and sharing an ungapped core, the major fluxes created by the two inductors of an LCL filter cancel out mostly in the common core.

This paper is an extension of our earlier publications [16], [17] which proposed a modified high-order filter design, named *L(LCL)*$_2$ filter, based on the conventional *LLCL* filter. This filter can reduce the harmonics at the switching frequency and multiples of the switching frequency while saving the total inductance and thereby results in size reduction of the filter. The most important role of the grid side inductor in the traditional *LLCL* filter is to decrease the harmonics around the twice of the switching frequency. In the new topology, this

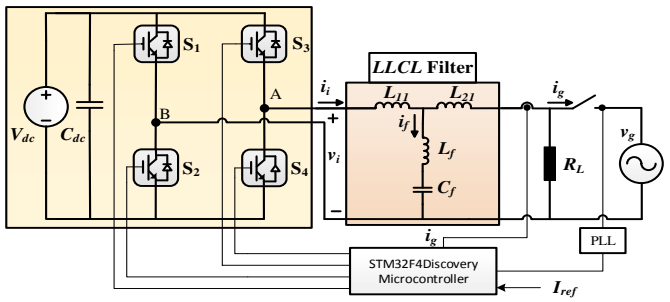

Fig. 1. Schematic diagram of the *LLCL* filter.

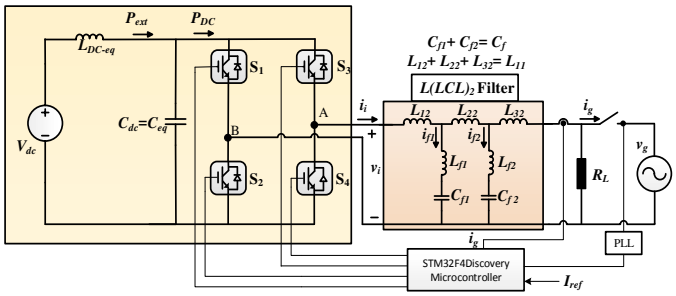

Fig. 2. Schematic of $L(LCL)_2$ system.

inductor is removed, and the converter side inverter of the filter is split into three parts. Then, two resonant traps at switching frequency and double of switching frequency are inserted in between the converter side inductor. The proposed filter is able to attenuate the current ripple components better than the *LCL* and traditional *LLCL* filters. This study can pave the path for the design and implementation of the *L(LCL)*$_2$ filter in VSI applications. This work has also presented the tools for further exploring the *L(LCL)*$_2$ filters for other case studies, such as analyzing the stability of the system, optimizing the filter parameters, designing damping methods and EMI suppressor for the filter, etc.

The outline of the rest of the paper is as follows. First, the principle of an *LLCL* filter is presented for a single-phase power converter. Next, the engineering design procedure of the *L(LCL)*$_2$ filter is proposed in Section II. Size estimation and efficiency analysis are presented in part B and C of Section II, respectively. In order to confirm the correctness of theoretical analysis, comparison of the simulation and experimental results for both *LLCL* and *L(LCL)*$_2$ filters are illustrated in Section II. Closed loop stability analysis of the current controller and the small-signal model of dc-link dynamics are studied in this section as well. Eventually, we conclude the paper in Section IV.

II. Parameter Design of the *L(LCL)*$_2$ Filter

The circuit configuration of an $LLCL$ and $L(LCL)_2$ filter-based single phase grid-tied VSI is shown in Figs. 1 and 2 respectively. The inverter output voltage and current of the *LLCL* filter are represented as v_i (between points *A* and *B*) and i_i, and the grid voltage and current are represented as v_g and i_g. The switching frequency is shown as f_s (in hertz) or ω_s (in radians per second). The power grid is assumed to be a perfect voltage source with zero impedance, to supply a continuous voltage at the frequency of $60Hz$. Fig. 4 shows the

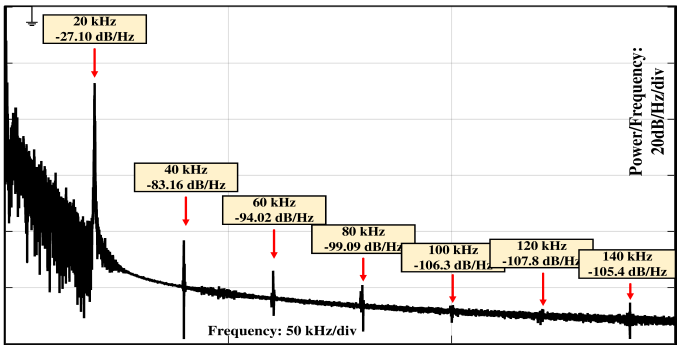

Fig. 3. Experimental power density spectrum of the inverter-side current when using unipolar modulation.

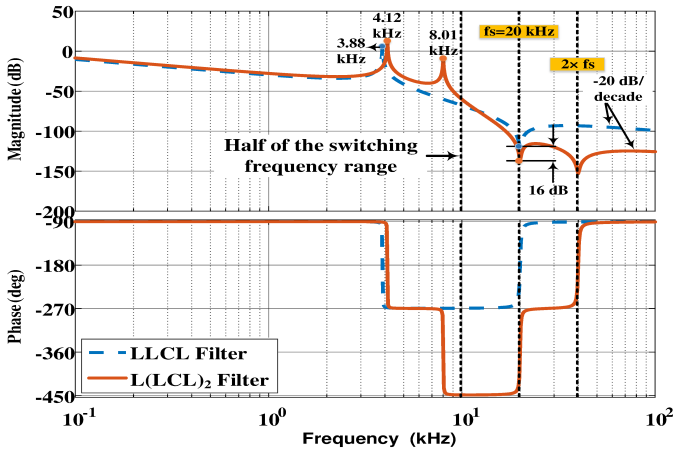

Fig. 4. Simulated Bode plots of transfer functions $i_g(s)/v_i(s)$.

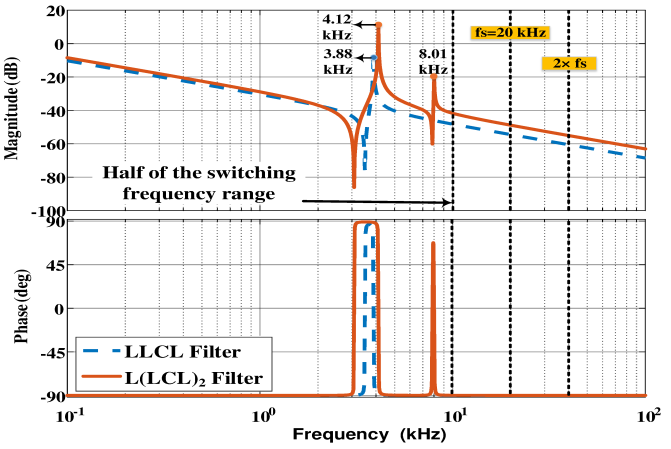

Fig. 5. Simulated Bode plots of transfer functions $i_i(s)/v_i(s)$.

main harmonic current power density spectrum of the inverter output current in the hardware setup, when the dc-link voltage V_{dc} is *220 V*, the modulation index, *m*, is *0.9*, inverter-side current ripple is $24.1\% I_{ref}$ (I_{ref} is fundamental peak current), and the switching frequency f_s is *20 kHz*. As can be seen, the topmost harmonics of inverter output current are around the switching frequency and then the multiples of switching frequency. Consequently, the paralleled trap $L_{f1}C_f$ is mainly limited by the harmonics around the switching frequency and the grid-side inductor L_{21} is limited by double of switching frequency [18].

Considering *A(s)* and *M(s)* definitions as below

$$A(s) = \frac{Z_2(s)Z_{f2}(s)}{Z_2(s) + Z_{f2}(S)}, M(s) = \frac{Z_2(s)}{Z_{f2}(s)} + 1 \quad (1)$$

where $Z_1(s) = sL_{12}$, $Z_2(s) = sL_{22} = sL_{32}$, $Z_{f1}(s) = sL_{f1} + 1/sC_{f1}$ and $Z_{f2}(s) = sL_{f2} + 1/sC_{f2}$. And assuming grid is an ideal sinusoidal voltage source, the transfer functions $i_1(s)/v_i(s)$ and the transfer functions $i_g(s)/v_i(s)$ of *L(LCL)*$_2$ filter can be, respectively, derived as [19]

$$\begin{aligned} G_{u_i \rightarrow i_i}(s) &= \frac{i_i(s)}{v_{i(s)}}|_{v_g(s)=0} \\ &= \frac{A + Z_2 + Z_{f1}}{(A + Z_2 + Z_1)Z_{f1} + (A + Z_2)Z_1} \end{aligned} \quad (2)$$

$$\begin{aligned} G_{u_i \rightarrow i_g}(s) &= \frac{i_g(s)}{v_{i(s)}}|_{v_g(s)=0} \\ &= \frac{Z_{f1}}{Z_2(M + Z_{f1}(M + Z_2) + 1) + MZ_1Z_{f1}} \end{aligned} \quad (3)$$

Fig. 4 shows bode plots of the transfer function $i_g(s)/v_i(s)$ of both the *L(LCL)*$_2$ filter and the *LLCL* filter while all the other parameters are the same except inductances of the traps. Also, the L_{11} in *LLCL* filter is divided into three parts and C_f is divided into two capacitors. Fig. 5 presents bode plots of the transfer function $i_i(s)/v_i(s)$ with aforementioned parameters. The figures help in verifying that all the requirements are satisfied with the design. It can be recognized that within half of the switching frequency range, the *L(LCL)*$_2$ filter has almost the same frequency response pattern of an *LLCL* filter and both resonant frequencies match the resonant frequency criteria of low pass filters for having a stable system. That is to say, compared to an ordinary *LLCL* filter, the additional $C_{f2}L_{f2}$ branch of the $L(LCL)_2$ filter does not bring any further control worries.

Some limitations are introduced by [5], [16], [17], [20] to be considered when designing power filters, that could be used in *L(LCL)*$_2$ filter.

1) The total capacitive reactive power at rated load should be less than 5% of the nominal power and capacitors are limited by this constraint.
2) The total inductance is limited by the voltage drop during the filter operation (lower than 10%). Otherwise, the dc-link voltage will be required to be higher to assure current controllability, which will result in greater losses in switching devices.
3) The range of the resonant frequency ought to be between ten times the line frequency or one-sixth of the switching frequency (whichever is bigger) [21] and one-half of the switching frequency, to keep away from stability and control problems may cause by resonance in the lower and upper parts of the harmonic spectrum.
4) The inverter-side inductor L_{12} is constrained by the requirement of the maximum ripple current (generally lower than 40%).
5) Considering *IEEE 519-2014*, harmonics upper than the 35^{th} should be limited. For a grid-tied inverter system, each of the harmonic currents of greater than the 35^{th} have to be less than 0.3% of the rated fundamental current, if the short-circuit current of the system is less than *20* times the nominal grid-side fundamental current.

Considering mentioned constraints, the *L(LCL)*$_2$ filter can be designed by using the following step by step procedure.

1) With the intention of meeting a specific current ripple requirement, the inductance can be designed from the equation
$$\frac{V_{dc}}{4f_s(\alpha_1 I_{ref})} \geq L_{11} \geq \frac{V_{dc}}{4f_s(\alpha_2 I_{ref})} \quad (4)$$
where I_{ref} is the rated reference peak current, α_1 and α_2 are the inverter-side current ripple ratio, which generally have the value of *15%* and *40%*, respectively. This inductance is the amount of total inductance of the filter ($L_{11} = L_{21} + L_{22} + L_{23}$) while $L_{21} = K \times L_{11}$ ($33\% < K < 60\%$) and $L_{22} = L_{23} = (L_{11} - L_{21})/2$.
2) By selecting the absorbtion of reactive power while the system is operating in rated conditions, the capacitor value can be determined.
$$C_f(Total) = xC_b \quad (5)$$
where x is a percentage of the reactive power absorbed at rated conditions ($x < 1$). The total capacitor value is limited by the below condition,
$$C_{max} = \frac{5\%P_{rated}}{{V_g}^2\omega_0} \quad (6)$$
then the capacitor of each branch is almost half of the total capacitor.
3) As $L_{f1}C_{f1}$ and $L_{f2}C_{f2}$ resonate at the switching frequency and the double of the switching frequency, then, L_{f1} and L_{f2} can be calculated as
$$\frac{1}{\sqrt{L_{f1}C_{f1}}} = \omega_{s1}, \frac{1}{\sqrt{L_{f2}C_{f2}}} = \omega_{s2} \quad (7)$$
where ω_{s1} is the switching frequency and ω_{s2} is twice the switching frequency in radians per second.
4) Grid side inductance L_{21}: in *LLCL* filters, L_{21} is mostly used to attenuate each harmonic around the twice of the switching frequency down to 0.3% and it can be articulated as in (17), where $J_1(2\pi\alpha), J_3(2\pi\alpha)$, and $J_5(2\pi\alpha)$ are the integrals of the Bessel function corresponding to the sideband harmonics at the frequency of $(2\omega_s + \omega_0), (2\omega_s + 3\omega_0)$, and $(2\omega_s + 5\omega_0)$.
$$J = max(|J_1(2\pi\alpha|), |J_3(2\pi\alpha|), |J_5(2\pi\alpha|) \quad (8)$$
$$\frac{(V_{dc}/\pi) \times J \times |G_{v_i \rightarrow i_g}(j2\omega s)|}{I_{ref}} \leq 0.3 \quad (9)$$
For an *L(LCL)*$_2$ filter, because of the additional L_fC_f resonate circuit, the current harmonics around the double of switching frequency satisfy the requirements of *IEEE 519-2014* with far more ease. Therefor, L_{21} is replaced by a portion of L_{11}.
5) The resonant frequency can be calculated by setting the dominator of equations (10) or (11) to zero, after

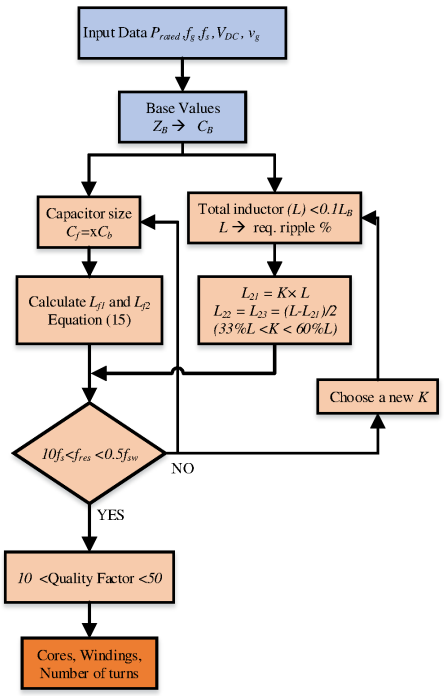

Fig. 6. Flowchart of the parameter design procedure of *L(LCL)*$_2$ filter.

replacing "*s*" with "$j\omega$". If it does not satisfy the requirement 3, absorbed reactive power can be changed and return to step 2. Or the tolerable current ripple can be adjusted again and return to step 1.

6) Quality factor of each resonant branch should be $10 \leq Q \leq 50$, which can be calculated as

$$Q = \frac{1}{R_f}\sqrt{\frac{L_f}{C_f}} \tag{10}$$

where R_f is the gaped equivalent resistance of the inductors in the resonant branches (L_{f1} and L_{f2}).

The most important limitations, such as the voltage drop across the inductor, the capacitive reactive power, and amplitude of the harmonic currents should be considered, while the design process is iterative with the *L(LCL)*$_2$ parameter values adjusted. The algorithm for designing the $L(LCL)_2$ filter is shown in Fig. 6.

A. Design example

Once designing a high-order filter for power inverters, the base impedance of the system should be identified. Thus, the base values of the total impedance, inductance, and capacitance are defined as (19)

$$Z_b = \frac{v_g}{P_{rated}}, L_b = \frac{Z_b}{\omega_b}, C_b = \frac{1}{\omega_b Z_b} \tag{11}$$

where ω_b is the grid frequency and P_{rated} is the rated active power of the inverter. Considering constrains addressed in section II−A, and under the condition of $f_s = 20kHz$, $V_{dc} = 220V$, $P_{rated} = 700W$, phase to ground voltage of the grid equal to *120 V/60 Hz*, and the sine-triangle asymmetrical regular sampled PWM, the *L(LCL)*$_2$ filter can be design by these steps,

1) Adopting the *7.7%* impedance for the inverter-side inductor, the inverter-side inductor is selected to be *4.2 mH*. For an *LLCL* filter, L_{21} mainly depends on the objective to attenuate each harmonic around the switching frequency down to *0.3%*, but for the *L(LCL)*$_2$ filter, owing to the $L_{f2}C_{f2}$ resonate circuit, the current harmonics around the twice of the switching frequency is approximately eliminated. Therefore, the calculated inductance for inverter side inductance of the traditional *LLCL* filter is split into three smaller inductances. The first part has a value of $L_{12} = 2.2mH$ (about *53%* of calculated inductance of *LLCL* filter) that can satisfy all requirements of grid side inverter, then $L_{22} = 1mH$ and $L_{32} = 1mH$.
2) The total capacitance to achieve maximum reactive power absorbed at rated conditions ($C_{f1} + C_{f2}$) $\leq$ *0.05* C_b , the capacitor value is designed to $C_{f1}+C_{f2} = 2\mu F$ to limit the reactive power to *1.55%*. If some of the constraints cannot be met, it should be increased to the limit of *5%*.
3) The grid-side inductor of L_{21} is removed in the *L(LCL)*$_2$ filter, but L_{22} and L_{23} are two sections of the split filter, and both has the value of *1mH*.
4) The consequent resonance frequency is *3.88 kHz* for the *LLCL* and the *L(LCL)*$_2$ filter has two resonant frequencies of *4.12 kHz* and *8.01 kHz*, which all are lower than one-half of the switching frequency and bigger than one-sixth of the switching frequency.
5) The quality factor of resonant branches is chosen to be *50*, and the equivalent resistor value of R_{f1} is 0.16Ω and R_{f2} is 0.08Ω.

B. Size Estimation of $LLCL$ and $L(LCL)_2$ Filters

Exact size approximation is challenging because of different manufacturing processes and design parameters. To generate an initial estimate, however, A number of methods were proposed for the size estimation of filter inductors and capacitors based on peak energy requirements. Although final recognitions probably will not obey this linear scaling, the component choice for inductor and capacitor volume with rated energy are accurate. The scaling factors are $1.11m^3/kj$ for inductive component and $0.54m^3/kj$ for capacitive component [22], a ratio of approximately *2* to *1*, where j stands for joules. In order to give an estimate of stored energy and size of the components, using the relationship $E_c = \frac{1}{2}CV^2$ and $E_L = \frac{1}{2}LI^2$, Table I is generated. By looking at Table I it is clear that the total size of the *LLCL* filter is $0.0656 \times 10^{-3}m^3$ and the total size of the $L(LCL)_2$ filter is $0.0546 \times 10^{-3}m^3$. Therefore, by implementing the $L(LCL)_2$ filter the size of the filter is reduced by the factor of 16.8%.

C. Efficiency comparison between the $LLCL$ and $L(LCL)_2$ Filters

The proposed $L(LCL)_2$ filter can be more attractive than an $LLCL$ filter as the interface between the inverter and the grid requires reduced copper and magnetic materials. The power losses of the filters can be separated into:

TABLE I
SIZE ESTIMATION OF *LLCL* AND $L(LCL)_2$ FILTERS

Components	Energy Stored in the Components (j)	Size of the components (m^3)
$L_{11}+L_{12}$	0.0919	0.0496×10^{-3}
L_f	1.29×10^{-7}	0.6966×10^{-10}
C_f	0.0144	0.016×10^{-3}
$L_{12}+L_{22}+L_{32}$	0.0715	0.0386×10^{-3}
$L_{f1}+L_{f2}$	8.09×10^{-8}	4.3686×10^{-11}
$C_{f1}+C_{f2}$	0.0144	0.016×10^{-3}

1) High-frequency passive damping loss, which can be obtained as follows

$$P_d(ripple)=\frac{1}{2}|I_{AM}(n,k_1)|^2\times R_{f1}+|I_{AM}(n,k_2)|^2\times R_{f2} \tag{12}$$

where $n=\pm1,\pm3,\pm5$, $k_1=1$ and $k_2=2$.

Passive Damping (PD) techniques use a resistance connected in series with the capacitor in order to attenuate the *LC* branch resonance at the cost of curtailing efficiency [23]. Lossless Active Damping (AD) methods with virtual resistors have been widely explored to suppress these oscillations. By using this technique, a resistance damping characteristic emulated in the lossless method, and no resistance is physically connected to the circuit [24]. Therefore, when using active damping method, P_d can be set to zero.

2) Power losses in inductors, can be separated into P_{core} (core loss) and P_{copper} (copper loss)

$$P_{core}=k(f^{\alpha}B^{\beta}V_e) \tag{13}$$

where *k*, α, and β are material parameters generally found by curve fitting; *B* is the flux density, in Tesla and V_e is the magnetic core volume, in cm^3.

$$P_{copper}=I_fR_{dc}^2+I_{ac}R_{ac}^2 \tag{14}$$

where I_f is the RMS value of the fundamental frequency current component and I_{ac} is the RMS value of the ac-ripple current component. it can be assumed that $R_{ac}=R_{dc}$ in this study. The power loss and efficiency values of the $L(LCL)_2$ filter and the $LLCL$ filter for both PD and AD methods are presented in Table II. It can be seen that the efficiency is increased by *0.169%* (for PD method) and *0.173%* (for AD method) compared to that of the *LLCL* filter.

The total loss of the $LLCL$ and $L(LCL)_2$ filters are measured in our hardware prototype by means of a *LaCroy WaveRunner 64Xi, 600 MHz Oscilloscope*. The measured output power was 691.55 watts for the $LLCL$ and 692.74 watts for $L(LCL)_2$ filter. The input power of both filters (which is the output power of the VSC) was 697.27 watts. The values in Table II are based on calculation, but the measured values of efficiencies are 99.17% and 99.35% for $LLCL$ and $L(LCL)_2$, respectively. Therefore, the measured total power losses for the $LLCL$ filter and the $L(LCL)_2$ filter are higher in value by a factor of 8.54 % and 10.63 %, respectively, comparing to calculated losses.

III. SIMULATION AND EXPERIMENTAL RESULTS

In order to confirm the effectiveness of the proposed *L(LCL)*$_2$ filter on suppressing the current harmonics, a 700-W prototype of the single-phase full-bridge grid-tied inverter with the "STM32F4" Microcontroller is constructed. In addition, a Matlab Simulink-based study is carried out to assess the experimental analysis. The experimental parameters of the filter are the same as those for simulations listed in Table III.

The experiments are evaluated and investigated under the given conditions of $f_s=20kHz$, $V_{dc}=220V$, $v_g=120V/60Hz$, $P_{rated}=700W$, and SPWM strategy is used in the inverter and the dc-link voltage is kept at $220V$.

Case I is the traditional *LLCL* filter strategy and Case II is the *L(LCL)*$_2$ filter strategy with an extra trap at $40kHz$. Figs. 7-11 show important system measurements that are captured by a LaCroy WaveRunner 64Xi oscilloscope in experimental tests and Matlab Simulink plots.

TABLE II
CALCULATED POWER LOSSES AND EFFICIENCY OF THE $L(LCL)_2$ FILTER AND THE *LLCL* FILTERS BASED ON NOMINAL OUTPUT POWER OF 700W.

	LLCL	$L(LCL)_2$
P_d	*0.0064w*	*0.0345w*
P_{copper}	*3.4432w*	*2.7593w*
P_{core}	*1.8238w*	*1.3015w*
Total Loss(PD)	***5.2735w***	***4.0953w***
Total Loss(AD)	***5.2671w***	***4.0608w***
Efficiency(PD)	*99.247%*	*99.415%*
Efficiency(AD)	*99.248%*	*99.420%*

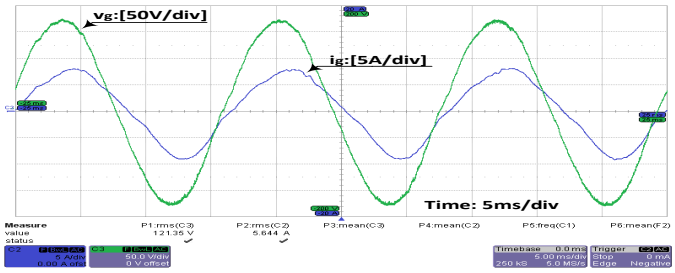

(a)

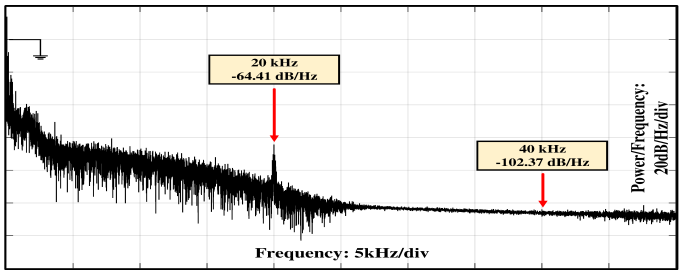

(b)

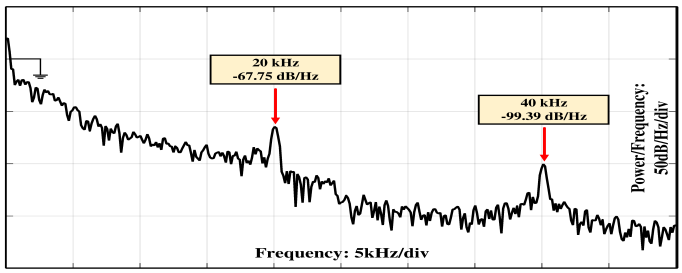

(c)

Fig. 7. *LLCL* filter. (a) Grid voltage and grid-side current waveforms. (b) Power density spectrum of grid-side current (Experimental setup). (c) Power density spectrum of grid-side current (Simulation)

This article has been accepted for publication in a future issue of this journal, but has not been fully edited. Content may change prior to final publication. Citation information: DOI 10.1109/TIA.2017.2712783, IEEE Transactions on Industry Applications

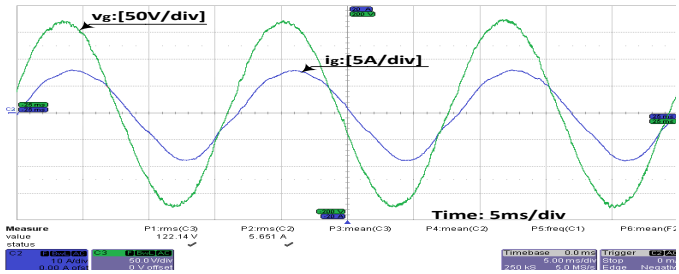

(a)

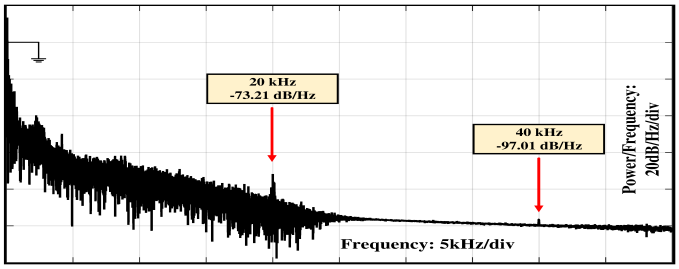

(b)

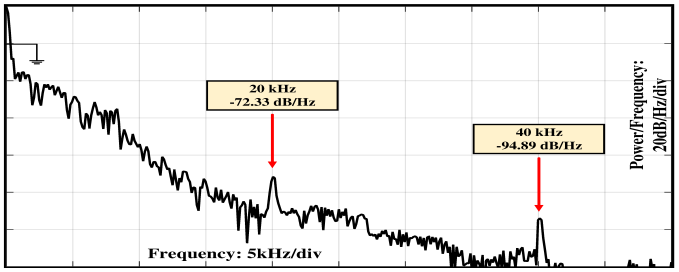

(c)

Fig. 8. *L(LCL)*$_2$ filter. (a) Grid voltage and grid-side current waveforms. (b) Power density spectrum of grid-side current (Experimental setup). (c) Power density spectrum of grid-side current (Simulation).

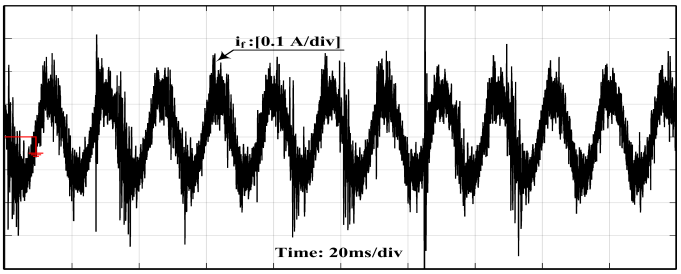

(a)

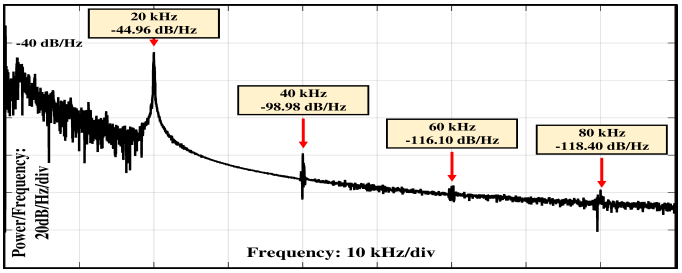

(b)

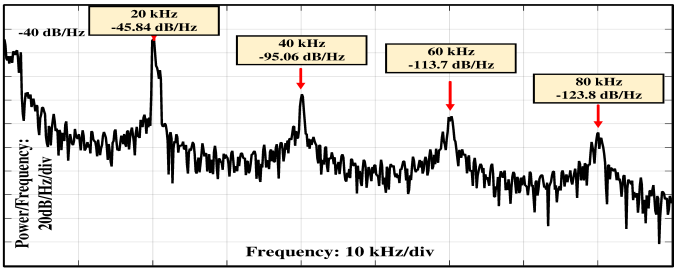

(c)

Fig. 9. (a) L_fC_f current of *LLCL* filter . (b) Power spectral density of L_fC_f current in *LLCL* filter (Experimental setup). (b) Power spectral density of L_fC_f current in *LLCL* filter (Simulation).

Figs. 7 and 8 show the grid side current-voltage waveforms and the power density spectrum of the grid-side current for cases I and II, respectively. Figs. 7(b) and Fig. 8(b) illustrate that the amplitude of the dominant harmonic current at *20 kHz* is reduced by *8.80 dB/HZ* from case I to case II, but at *40 kHz* it increased from *-102.37 dB/Hz* (case I) to *-97.01 dB/Hz* (case II). Therefore, the most dominant current harmonics are diminished even more than the previous design. However, a small increase occurred at the double of the switching frequency, but as the power density is too small (*-97.01 dB/Hz*), it can be neglected. Thus, the size of the filter is reduced, and as a result, the total loss is decreased. In addition, the performance of the filter is improved. Figs. 7 (c) and 8 (c) show the simulation results of the power density spectrum of the grid-side current. As it can be seen, the experimental results are in accordance with the simulation graphs.

The currents flowing through the resonant branches for Case I and Case II are shown in Figs. 9 to 11 while the grid current is *5.8 A* and the voltage is *120 V*. The magnitude of the currents in $L_{f1}C_{f1}$ and $L_{f2}C_{f2}$ traps are almost half of L_fC_f trap and that is because the impedance of both traps of $L(LCL)_2$ filter is $2.652k\Omega$ (at *60 Hz*), but the *LLCL* filter has an impedance of 1.326 kΩ. Also, it can be seen that the power density of current harmonics at the switching frequency and multiples of the switching frequency are almost the same in the L_fC_f branch of the *LLCL* and $L_{f1}C_{f1}$ branch of the $L(LCL)_2$ filter. In addition to that more attenuation occurs at $L_{f2}C_{f2}$. Then, in Figs. 9 (c) - 11 (c) simulation results are depicted which are quite close to the hardware experimental results.

The measured total harmonic distortion *(THD)%* of i_g in Cases I, and II are *3.72%* and *2.94%* which shows the effectiveness of the designed filter in improving the THD of the grid current.

At last, the response of the developed filter is compared with that of an *LLCL*-based inverter in terms of voltage regulation. In order to do that, the simulations were run at a sampling time of $2\mu s$ and the values of Table III. These values were designed such that the performance of the $L(LCL)_2$ filter is comparable to that of the *LLCL* in terms of steady state performance and the dynamic response. Fig. 12 shows both cases when a $0.5pu$ load is switched in at the point of grid connection on $t = 0.15s$. It can be seen that the inverter maintains a constant dc-link voltage before and after the change. Results show that, replacing the *LLCL* filter with an $L(LCL)_2$ filter improves the dynamic performance of the inverter mainly due to the reduction of dc-link voltage fluctuations.

The experimental setup of the *L(LCL)*$_2$-filter-based inverter system is shown in Fig. 13. For building the inductances of *LLCL* and *L(LCL)*$_2$ filters Ferrite cores with N87 material and epoxy coating is used.

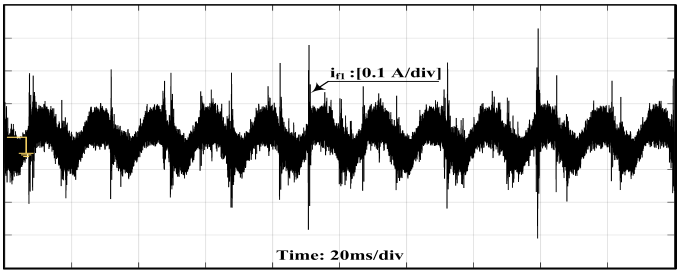

(a)

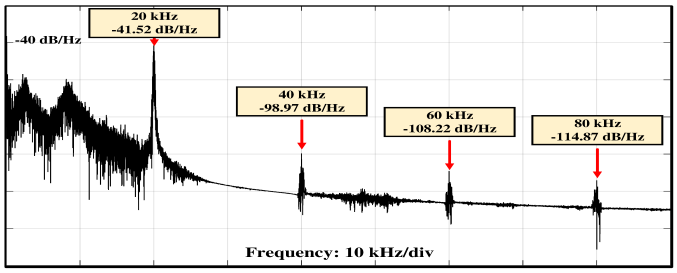

(b)

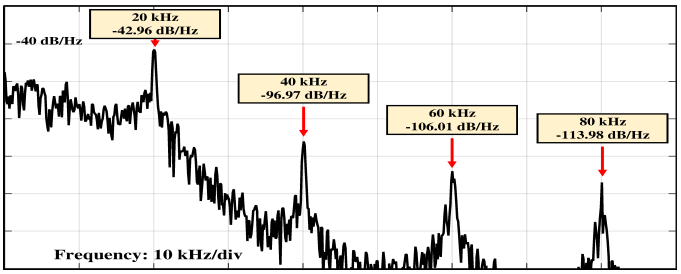

(c)

Fig. 10. (a) Current of switching frequency trap $L_{f1}C_{f1}$ of $L(LCL)_2$ filter. (b) Power spectral density of $L_{f1}C_{f1}$ current in *L(LCL)*$_2$ filter (Experimental setup). (c) Power spectral density of $L_{f1}C_{f1}$ current in *L(LCL)*$_2$ filter (Simulation).

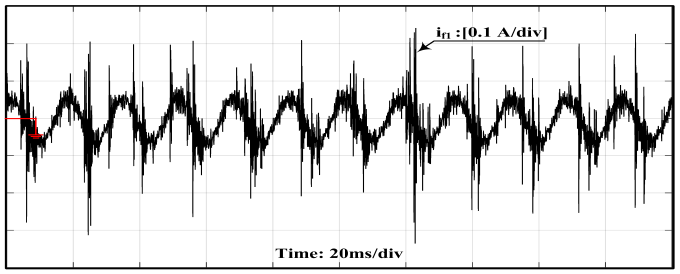

(a)

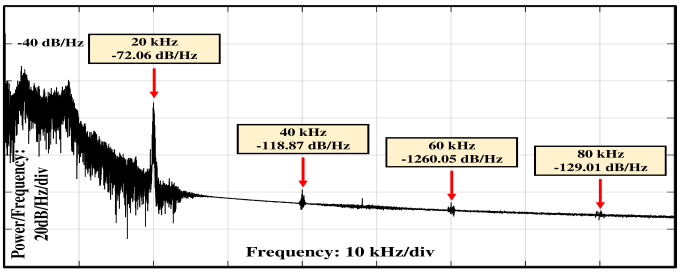

(b)

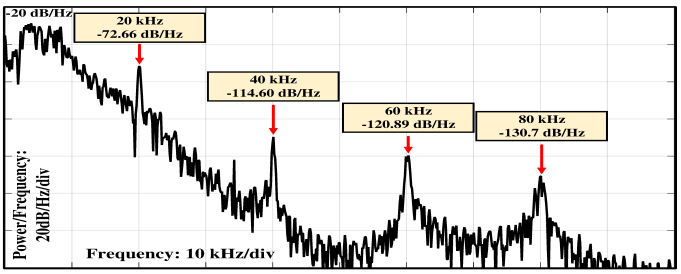

(c)

Fig. 11. (a) Current of the double of switching frequency trap $L_{f2}C_{f2}$ of *L(LCL)*$_2$ filter . (b) Power spectral density of $L_{f2}C_{f2}$ current in *L(LCL)*$_2$ filter (Experimental setup). (c) Power spectral density of $L_{f2}C_{f2}$ current in *L(LCL)*$_2$ filter (Simulation).

A. Analysis and Discussion

From the simulation and experimental results, the following can be seen.

1) In both cases, dominating harmonic current meets the recommendation of *IEEE 519-2014* in the experiment, however, the *20kHz* current harmonic reduced and the *40kHz* current harmonic has the same value.
2) The value of the grid-side inductor is reduced in cases II, so the voltage drop during the operation and thereby the dc link voltage are the same.
3) The value of the total inductor of $L(LCL)_2$ filter is reduced by a factor of *22.22%*, compared to that of the *LLCL* filter.
4) The reactive power in the newly designed filter is the same as the traditional *LLCL* filter $C_{f1} + C_{f2} = C_f$.
5) In general, the experimental results are in acceptable agreement with the theoretical study, particularly with regard to the harmonic current attenuation around the switching frequency and the double of the switching frequency.

B. Close-Loop Stability Analysis of the Current Controller

The eigenvalue analysis is one of the suitable techniques that can be used for the stability analysis of a system. Fig. 14 illustrates the general block diagram of a current controller,

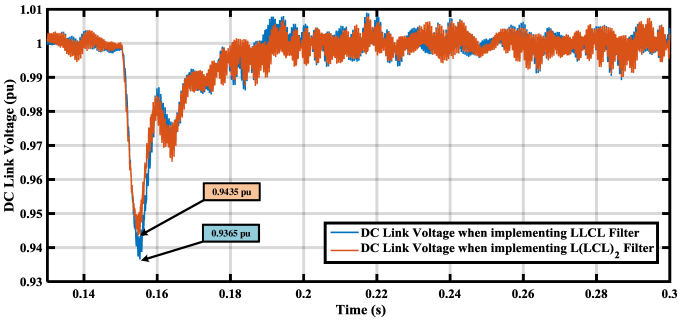

Fig. 12. DC Link voltage when a 0.5 pu load is switched-in on t=0.15.

where P(s), C(s), and G(s) are the model of the controller, inverter, and proposed filter, respectively. A conventional PI controller is adopted as P(s) to obtain the dynamics, i.e.

$$P(s) = \frac{(k_p s + k_I)}{s}. \tag{15}$$

where k_p = 1 is proportional gain and k_I = 100 is the integral gain. These values are designed and tuned by the trial and error method. It is assumed that the time delays in the system because of the phasor PWM blocks are negligible, i.e., *C(s)=1*, and *G(s)* is calculated by (3). Therefore, the closed-

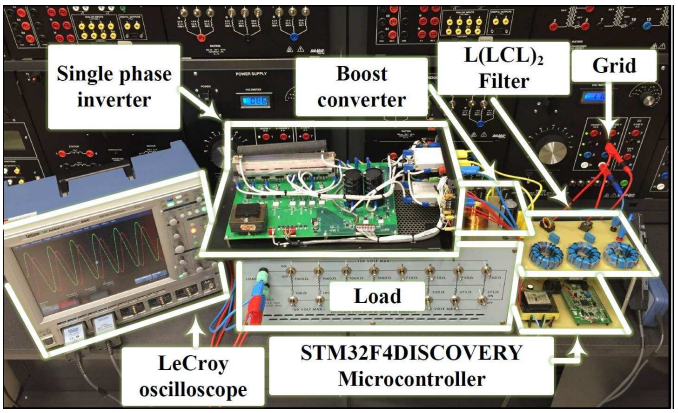

Fig. 13. Experimental Setup

TABLE III
PARAMETERS USED FOR SIMULATIONS

Elements	Parameters	Values
Inverter	DC link voltage (V_{dc})	*220 V*
	Switching frequency (f_s)	*20 kHz*
	Rated power (P_{rate})	*700 w*
AC Grid	Grid phase voltage (V_g)	*120 V*
	Grid frequency (f_0)	*60 Hz*
$LLCL_2$ Filter	Converter side inductor (L_{12})	*2.2mH*
	Grid side inductors ($L_{22} = L_{32}$)	*1 mH*
	Resonant circuit inductor (L_{f1})	$63.3\mu H$
	Resonant circuit inductor (L_{f2})	$15.83\mu H$
	Resonant circuit capacitors ($C_{f1} = C_{f2}$)	$1\mu F$
	Equivalent resistance of the inductor (R_{f1})	0.16Ω
	Equivalent resistance of the inductor (R_{f2})	0.08Ω
LLCL Filter	Converter side inductor (L_{11})	*4.2 mH*
	Grid side inductor (L_{21})	*1.2 mH*
	Resonant circuit inductor (L_f)	$31.67\mu H$
	Resonant circuit capacitor (C_f)	$2\mu F$
	Equivalent resistance of the inductor (R_f)	0.11Ω

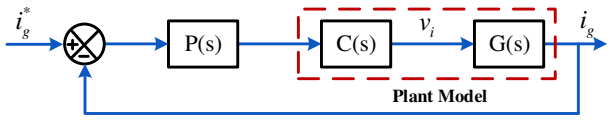

Fig. 14. Block diagram of the current control system.

loop transfer function of the current control system can be written as

$$H(s) = \frac{i_g(s)}{i_g^*(s)} = \frac{P(s)G(s)}{1 + P(s)G(s)} \tag{16}$$

The bandwidth of a closed-loop control system is defined as the frequency range where the magnitude of the closed loop gain does not drop below -3 dB, as shown in Fig 15. As can be seen, the bandwidth of closed-loop transfer function of the current controller with the proposed $L(LCL)_2$ filter is around 120 Hz.

It is assumed that the time delays in the system because of the phasor PWM blocks are negligible. The eigenvalues of the closed-loop transfer function determine the dynamics of the closed-loop system. Here, the stability of the proposed system, with respect to the variation in the proposed *L(LCL)*$_2$ parameters, is studied. This study is based on a *700 w* laboratory prototype, in which parameters are summarized in Table I. The eigenvalues of the system at this operating point

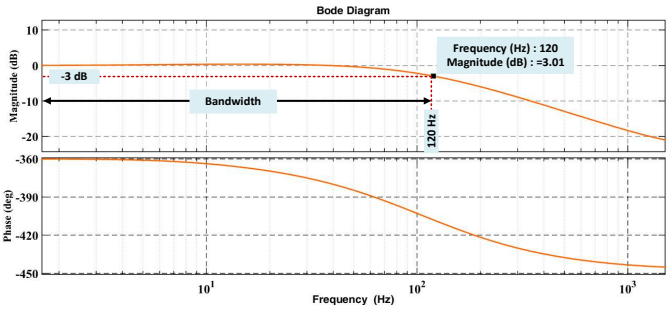

Fig. 15. Closed-loop frequency response of the current controller indicating the bandwidth and the cutoff frequency.

are $\lambda_{1,2} = -118.78 \pm j99.22$, $\lambda_{3,4} = -286.43 \pm j25867.9$, and $\lambda_{5,6} = -1403.46 \pm j50321.53$. The real parts of all six eigenvalues are negative, which betokens the stability of the linearized system. However, the stability of the overall system cannot be guaranteed for all values of the filter parameters. Thus, for stability analysis, the eigenvalues of the system are plotted versus the variation of one parameter at a time, while the other nominal parameters remain constant.

It should be noted that the range variation of all filter parameters correspond to the step by step design procedure discussed in Section III. Moreover, in transfer function (16), with $\pm 20\%$ variations of the L_{f1} and the L_{f2}, the system eigenvalues remain almost constant. Indeed, the variation of L_{f1} and L_{f2} does not affect the stability of the proposed system.

Fig. (16a) and Fig. (16b) show the impacts of L_{12} and L_{32} on the eigenvalues of the system, respectively, when L_1 varies from 1.39 mH to 2.52 mH and L_{32} varies from 0.84 mH to 1.485 mH. Since L_{22} is equal to L_{32}, their variations are depicted together in Fig. (16b). It can be observed that the increase of the converter-side and the grid-side inductance moves all eigenvalues into the vertical axis. Thus, once L_{12} and L_{32} increase, it is expected that the overall system response becomes longer and less oscillatory.

The variation of the system eigenvalues by varying the C_{f1} and C_{f2} from 0.5 μF to 3 μF are shown in Fig. (16c) and Fig. (16d). As can be seen, the impact of the C_{f1} and C_{f2} on the eigenvalues λ_1 and λ_2 are almost negligible. However, Fig. (16c) depicts that complex eigenvalues λ_3, λ_4, λ_5, and λ_6 move into the real axis, which can decrease the natural frequencies of the system and increases the damping factor of the system. Fig. (16d) determines that all eigenvalues stay on the left half of the s-plane for the whole operating range that demonstrates the stability of the system over the given range.

Figs. (16e) and (16f) illustrate the eigenvalues of the proposed system as R_{f1} and R_{f2} vary from 0.08 Ω to 0.39 Ω and 0.16 Ω to 0.8 Ω, respectively. As can be seen, increasing the resistances of the filter moves the real part of eigenvalues λ_3, λ_4, λ_5, and λ_6 toward the left, resulting in faster response and less oscillatory.

C. Small-signal model of the dc-link dynamics considering the instantaneous power for bi-directional ac/dc power flow applications

If the *L(LCL)*$_2$ filter is employed in bi-directional ac/dc power flow applications, the converter should be able to

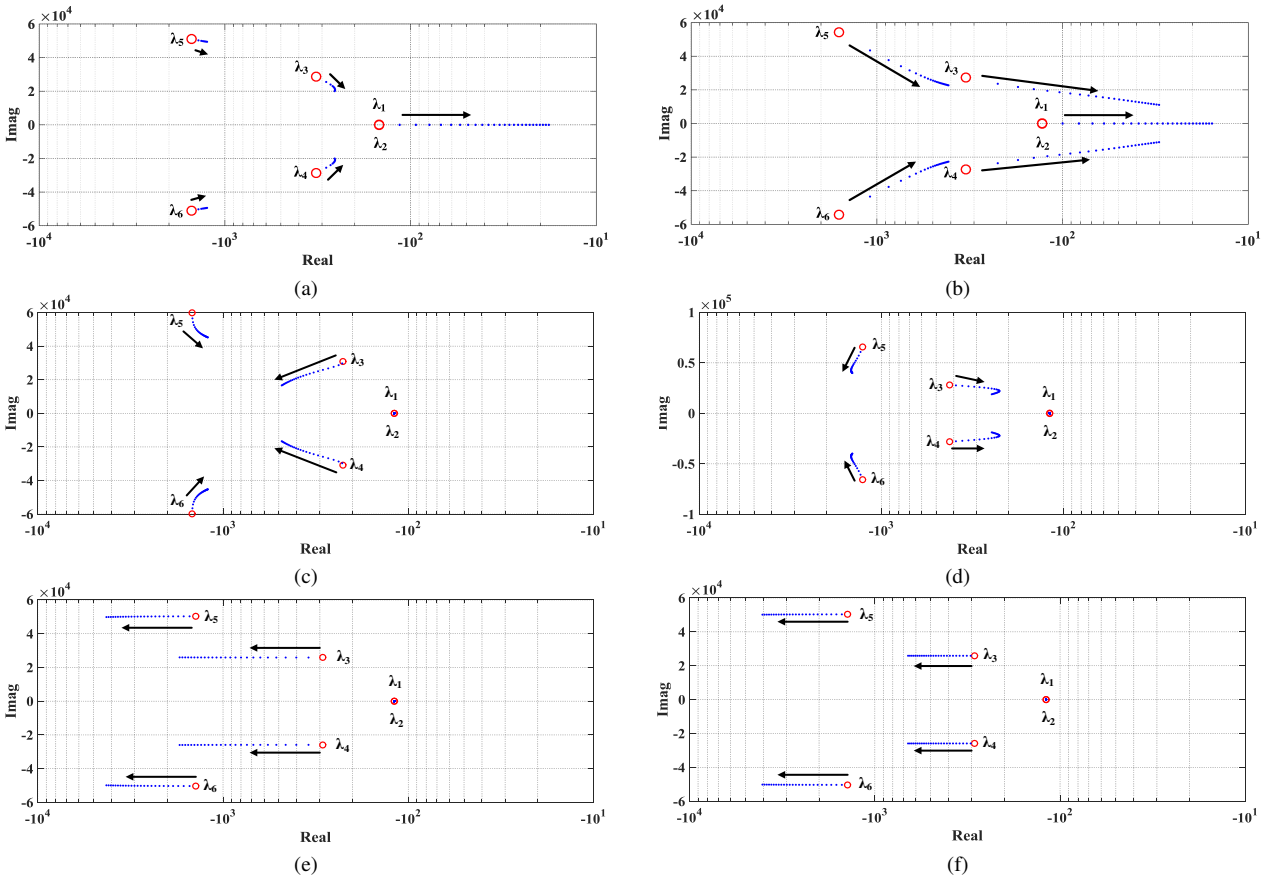

Fig. 16. Root locus of the closed-loop transfer function of the current controller (H_s) as (a) L_{12} varies from 1.39mH to 2.52mH (b) L_{22} and L_{32} vary from 0.84mH to 1.485mH (c) C_{f1} varies from 0.5μF to 3μF (d) C_{f2} varies from 0.5μF to 3μF (e) R_{f1} varies from 0.08Ω to 0.39Ω. (f) R_{f2} varies from 0.16Ω to 0.8Ω.

regulate dc voltage, and the instantaneous power stored in the ac side filter affects the dc side dynamics. In this section, the small-signal model of the dc-link dynamics considering the instantaneous power is studied.

In high-order ac-side filters applications, e.g. LCL, $LLCL$ or $L(LCL)_2$ filter due to the frequency-scale separation of the high order filter dynamics and dc-link voltage dynamics, the filter has a negligible effect on the dc-link voltage dynamics. The fundamental frequency is normally higher than the bandwidth of the dc-link voltage control loop (between 20 to 50 Hz). The high order ac-side filter acts mainly as an L filter ($L_{12}+L_{22}+L_{32}$) [25].

The dc-link dynamics' model can be obtained when the total instantaneous power in storage devices, i.e., $L_{\mathrm{DC-eq}}$ and C_{eq} are considered. The calculations on this section are based on [26] and [27]. C_{eq} and $L_{\mathrm{DC-eq}}$ are the equivalent capacitance and inductance reflected to the dc side VSC, respectively. The power balance across the dc-link capacitor can be given by:

$$\begin{aligned} P_{\mathrm{ext}} \quad - \quad & P_{\mathrm{loss}} - \frac{V_{\mathrm{DC}}^2}{R_L} - D\left(0.5 L_{\mathrm{DC-eq}} I_{\mathrm{DC}}^2\right) \\ & - D(0.5 C_{\mathrm{eq}} V_{\mathrm{DC}}^2) = P_{\mathrm{DC}} = P_t \end{aligned} \tag{17}$$

where I_{DC} is the current of the dc inductor; P_{ext} is the external injected power to the dc side; P_{loss} is the losses in the converter; R_L is the VSC reflected dc side equivalent static resistance; P_{DC} is the net power as shown in Fig 2, that is equivalent to the VSC ac-side power P_t; and the time-derivative operator is represented by D - i.e., $Dx = d(x)/dt$. Consider that Pt does not have the same value of the grid injected power (P_s), because of the ac-side filter.

By using similar calculation in [26] and letting $x_1 = V_{\mathrm{DC}}$ and $x_2 = DV_{\mathrm{DC}}$; the power balance equation can be calculated as follows

$$\begin{aligned} \tilde{P}_{\mathrm{ext}} \quad - \quad & \tilde{P}_{\mathrm{loss}} - \tilde{P}_{\mathrm{DC}} - L_{\mathrm{DC-eq}} C_{\mathrm{eq}} \frac{P_{\mathrm{DC-0}}}{V_{\mathrm{DC-nominal}}} \tilde{D} x_2 \\ & - L_{\mathrm{DC-eq}} \frac{P_{\mathrm{DC-0}}}{V_{\mathrm{DC-nominal}}^2} \tilde{D} P_{\mathrm{DC}} \\ & + L_{\mathrm{DC-eq}} \frac{P_{\mathrm{DC-0}}^2}{V_{\mathrm{DC-nominal}}^3} \tilde{x}_2 - C_{\mathrm{eq}} V_{\mathrm{DC-nominal}} \tilde{x}_2 \\ & - \frac{2 V_{\mathrm{DC-nominal}}}{R_p} \tilde{x}_1 = 0. \end{aligned} \tag{18}$$

where ˜ indicates the perturbed signal around the equilibrium point (E.P.) of each variable. Moreover, the equilibrium point (E.P.) can be expressed by (19) taken into account that all variables are static at the equilibrium situation

$$\begin{aligned} &(\text{E.P.}) = (x_{1-0}, x_{2-0}, Dx_{2-0} P_{\mathrm{DC-0}}, D P_{\mathrm{DC-0}}, P_{\mathrm{ext-0}}, \\ &P_{\mathrm{loss-0}}) = (V_{\mathrm{DC-nominal}}, 0, 0, P_{\mathrm{DC-0}}, 0, P_{\mathrm{ext-0}}, P_{\mathrm{loss-0}}) \end{aligned} \tag{19}$$

According to the equation (18), with the purpose of reaching a linear time-invariant (LTI) model that can describe the connection between the output V_{DC} and the control input I_g, a formula which connects P_{DC} to the control input I_g have to be calculated.

Therefore, studying the total power balance on the ac side is necessary for analyzing the instantaneous power of the ac-side filter. This power balance is defined as follows

$$P_{\rm DC} = P_t = P_{\rm loss\_R} + P_{\rm filter\_L} + P_s \tag{20}$$

where $P_{\rm loss\_R}$ is the total instantaneous power loss in the equivalent resistance of the inductor L_{12}, L_{22} and L_{32}, P_{loss_L} is the total instantaneous power of the ac-side inductor ($L_{12}+L_{22}+L_{32}$) , and P_s is the total absorbed/injected instantaneous power at the point of common coupling (PCC) for stabilizing the dc-link voltage. The total absorbed instantaneous power by a single phase network can be shown by

$$P_{\rm single\,phase\,network} = {\rm Re}\left\{\vec{v}(t)\vec{i}^{*}(t)\right\} \tag{21}$$

the total stored energy in filter inductors is expressed by

$$W_L = 0.5(L_{12}+L_{22}+L_{32})(i_g^2) \tag{22}$$

where i_g is the current injected into the inductors L_{12}, L_{22} and L_{32}. As a result, (23) is the expression of the instantaneous power of filter series inductors.

$$P_{\rm filter\_L} = (L_{12}+L_{22}+L_{32})i_g D i_g. \tag{23}$$

and P_s can be calculated by:

$$P_s = I_g V_{g_s} \tag{24}$$

where V_{g_s} is the voltage space vector at the PCC. Using (20) - (24), the relationship between P_{DC}, I_g can be shown by

$$\begin{aligned} P_{\rm DC} - (L_{12}+L_{22}+L_{32})i_g D i_g - R(I_g)^2 - I_g V_{g_s} \\ = G(I_g, DI_g) = 0. \end{aligned} \tag{25}$$

Equation (25) is nonlinear, therefore the Taylor series expansion around one E.P. is applied on the dynamic function G as

$$\begin{aligned} G(I_g, DI_g) &= G|_{\rm (E.P.)} + \frac{\partial G}{\partial I_g}|_{\rm (E.P.)}\tilde{I}_g \\ &\quad + \frac{\partial G}{\partial DI_g}|_{\rm (E.P.)}\tilde{D}I_g + \{\text{H.O.T.}\}. \end{aligned} \tag{26}$$

The E.P. of (26) can be shown by

$$\text{(E.P.)} = (I_{g-0}, DI_{g-0}) = (I_{g-0}, 0). \tag{27}$$

After mathematical manipulation, (28) can be reached.

$$\tilde{P}_{\rm DC} = LI_{g-0}\tilde{D}I_g + RI_{g-0}\tilde{I}_g + V_{g_s}\tilde{I}_g. \tag{28}$$

In addition to (28), $D\tilde{P}_{\rm DC}$ is also required to find the explicit transfer function between I_g and V_{DC} using (18). Using (28), $D\tilde{P}_{\rm DC}$ and its E.P. can be given by

$$\begin{aligned} DP_{\rm DC} &- (L_{12}+L_{22}+L_{32})((DI_g)^2 + I_g D^2 I_g) \\ &- 2RI_g DI_g - V_{g_s} DI_g \\ &= H(I_g, DI_g, D^2 I_g) = 0 \end{aligned} \tag{29}$$

$$\begin{aligned} \text{(E.P.)} &= (I_{g-0}, DI_{g-0}, D^2 I_{g-0}) \\ &= (I_{g-0}, 0, 0). \end{aligned} \tag{30}$$

By implementing the Taylor series expansion on the function H in (29), $D\tilde{P}_{\rm DC}$ can be calculated by

$$\begin{aligned} D\tilde{P}_{\rm DC} &= (L_{12}+L_{22}+L_{32})I_{g-0}D^2\tilde{I}_g + RI_{g-0}D\tilde{I}_g \\ &+ V_{g_s}D\tilde{I}_g. \end{aligned} \tag{31}$$

By combining the equations (18), (28), and (31), the relationship between I_g and V_{DC} is reached as follows

$$\begin{aligned} \tilde{V}_{\rm DC} &= \frac{\tilde{P}_{\rm ext} - \tilde{P}_{\rm loss}}{As^2+Bs+E} - \frac{as^2+bs+e}{As^2+Bs+E}\tilde{I}_g \\ a &\triangleq -L_{\rm DC-eq}(L_{12}+L_{22}+L_{32})\frac{P_{\rm DC-0}I_{g-0}}{V^2_{\rm DC-nominal}} \\ b &\triangleq -(L_{12}+L_{22}+L_{32})I_{g-0} \\ &- L_{\rm DC-eq}\frac{P_{\rm DC-0}}{V^2_{\rm DC-nominal}}(RI_{g-0}+V_{g_s}) \\ e &\triangleq -RI_{g-0} - V_{g_s} \\ A &\triangleq L_{\rm DC-eq}C_{\rm eq}\frac{P_{\rm DC-0}}{V_{\rm DC-nominal}} \\ B &\triangleq \left(C_{\rm eq}V_{\rm DC-nominal} - L_{\rm DC-eq}\frac{P^2_{\rm DC-0}}{V^3_{\rm DC-nominal}}\right) \\ E &\triangleq \left(\frac{2}{R_L}V_{\rm DC-nominal}\right) \end{aligned} \tag{32}$$

In many different references, e.g. [28], the effect of the dc filter is not taken into consideration, while the ac filter instantaneous power is reflected into the dynamic analysis of the dc-link voltage. In that situation, $L_{\rm DC-eq}$ is set to zero which results in (33) becoming a special case of (32). The values of a, b, e, A, B, and E are given in (33) for $L_{\rm DC-eq} = 0$.

$$\begin{aligned} a &= 0 \\ b &= -(L_{12}+L_{22}+L_{32})I_{g-0} \\ e &\triangleq -RI_{g-0} - V_{g_s} \\ A &= 0 \text{ then} \\ \tilde{V}_{\rm DC} &= \frac{-(L_{12}+L_{22}+L_{32})I_{g-0}s - V_{g_s} - RI_{g-0}}{C_{\rm eq}V_{\rm DC-nominal}s + \frac{2}{R_L}V_{\rm DC-nominal}}\tilde{I}_g \\ &\quad - \text{Disturbance Signals}. \\ B &= C_{\rm eq}V_{\rm DC-nominal} \\ E &= \frac{2}{R_L}V_{\rm DC-nominal} \end{aligned} \tag{33}$$

In (33), in both rectification and inversion modes, the magnitude of the linearized plant is the same. On the other hand, in the rectification mode, the phase is dramatically reduced at the same power, due to the right-hand-plane (RHP) zero. If the time constant of the current controller is equal to zero, in order to have a stable transfer function B and E in (33) should be positive. As $C_{\rm eq}$, $V_{\rm DC-nominal}$ and R_L are always positive numbers, (33) is always stable in bidirectional ac/dc power flow application.

IV. Conclusion

In this paper, the principle of the conventional *LLCL* filter and parameter design of the *L(LCL)$_2$* filters has been proposed. Since grid-side inductance (L_{21}) of the *LLCL* filter is mainly decided by the harmonic currents around the double of the

switching frequency instead of those around the switching frequency, it has been replaced by a small trap at double of the switching frequency. Compared to the *LLCL* filter, this replacement results in the reduction of the total inductance size and hence the total loss of the filter. The inverter side inductance is divided into three parts to place resonant branches in between them. Therefore, the $L(LCL)_2$ filter has less copper loss and better performance at high order harmonics attenuation. In the proposed design, the maximum power factor variation remained unchanged and the THD has improved by *18.61%*.

A *700 W* single-phase grid-tied inverter is designed to compare the characteristics of the conventional *LLCL* filter and the suggested $L(LCL)_2$ filter through experimental results. The results validate the value of the inductors of the $L(LCL)_2$ filter, which is reduced by a factor of *22.22%*, compared to that of the *LLCL* filter, when the modulation index is *0.9*.

Closed loop stability analysis of the current controller and the small-signal model of dc-link dynamics considering the instantaneous power for bi-directional ac/dc power flow applications have shown that the filter can perform stably in the same ranges of the *LLCL* filter.

REFERENCES

[1] A. Anzalchi and A. Sarwat, "Analysis of carbon tax as an incentive toward building sustainable grid with renewable energy utilization," in *Green Technologies Conference (GreenTech), 2015 Seventh Annual IEEE*, April 2015, pp. 103–109.

[2] A. Anzalchhi and A. Sarwat, "Artificial neural network based duty cycle estimation for maximum power point tracking in photovoltaic systems," in *SoutheastCon 2015*, April 2015, pp. 1–5.

[3] N. Harischandrappa and A. K. S. Bhat, "A fixed-frequency lcl -type series resonant converter with a capacitive output filter using a modified gating scheme," *IEEE Transactions on Industry Applications*, vol. 50, no. 6, pp. 4056–4064, Nov 2014.

[4] M. Lindgren and J. Svensson, "Connecting fast switching voltage source converters to the grid-harmonic distortion and its reduction," in *Stockholm Power Tech. Conf.*, June 18-22 1995, pp. 191–195.

[5] M. Liserre, F. Blaabjerg, and S. Hansen, "Design and control of an lcl-filter-based three-phase active rectifier," *Industry Applications, IEEE Transactions on*, vol. 41, no. 5, pp. 1281–1291, Sept 2005.

[6] I. Gabe, V. Montagner, and H. Pinheiro, "Design and implementation of a robust current controller for vsi connected to the grid through an lcl filter," *Power Electronics, IEEE Transactions on*, vol. 24, no. 6, pp. 1444–1452, June 2009.

[7] A. Reznik, M. G. Sim?es, A. Al-Durra, and S. M. Muyeen, "Lcl filter design and performance analysis for grid-interconnected systems," *IEEE Transactions on Industry Applications*, vol. 50, no. 2, pp. 1225–1232, March 2014.

[8] A. Houari, H. Renaudineau, J. P. Martin, B. Nahid-Mobarakeh, S. Pierfederici, and F. Meibody-Tabar, "Large-signal stabilization of ac grid supplying voltage-source converters with lcl-filters," *IEEE Transactions on Industry Applications*, vol. 51, no. 1, pp. 702–711, Jan 2015.

[9] P. Channegowda and V. John, "Filter optimization for grid interactive voltage source inverters," *Industrial Electronics, IEEE Transactions on*, vol. 57, no. 12, pp. 4106–4114, Dec 2010.

[10] Y. Jiao, S. Lu, and F. Lee, "Switching performance optimization of a high power high frequency three-level active neutral point clamped phase leg," *Power Electronics, IEEE Transactions on*, vol. 29, no. 7, pp. 3255–3266, July 2014.

[11] W. Wu, Y. Sun, Z. Lin, Y. He, M. Huang, F. Blaabjerg, and H.-H. Chung, "A modified llcl filter with the reduced conducted emi noise," *Power Electronics, IEEE Transactions on*, vol. 29, no. 7, pp. 3393–3402, July 2014.

[12] W. Wu, Y. Sun, M. Huang, X. Wang, H. Wang, F. Blaabjerg, M. Liserre, and H.-H. Chung, "A robust passive damping method for llcl-filter-based grid-tied inverters to minimize the effect of grid harmonic voltages," *Power Electronics, IEEE Transactions on*, vol. 29, no. 7, pp. 3279–3289, July 2014.

[13] W. Wu, Y. Sun, Z. Lin, T. Tang, F. Blaabjerg, and H.-H. Chung, "A new lcl -filter with in-series parallel resonant circuit for single-phase grid-tied inverter," *Industrial Electronics, IEEE Transactions on*, vol. 61, no. 9, pp. 4640–4644, Sept 2014.

[14] D. Pan, X. Ruan, C. Bao, W. Li, and X. Wang, "Capacitor-current-feedback active damping with reduced computation delay for improving robustness of lcl-type grid-connected inverter," *Power Electronics, IEEE Transactions on*, vol. 29, no. 7, pp. 3414–3427, July 2014.

[15] D.Pan, X.Ruan, C.Bao, W.Li, and X.Wang, "Magnetic integration of the lcl filter in grid-connected inverters," *Power Electronics, IEEE Transactions on*, vol. 29, no. 4, pp. 1573–1578, April 2014.

[16] W. Wu, Y. He, and F. Blaabjerg, "An llcl power filter for single-phase grid-tied inverter," *Power Electronics, IEEE Transactions on*, vol. 27, no. 2, pp. 782–789, Feb 2012.

[17] A. Anzalchi, M. Moghaddami, A. Moghaddasi, A. I. Sarwat, and A. K. Rathore, "A new topology of higher order power filter for single-phase grid-tied voltage-source inverters," *IEEE Transactions on Industrial Electronics*, vol. 63, no. 12, pp. 7511–7522, Dec 2016.

[18] Y. Lang, D. Xu, S. Hadianamrei, and H. Ma, "A novel design method of lcl type utility interface for three-phase voltage source rectifier," in *Power Electronics Specialists Conference, 2005. PESC '05. IEEE 36th*, June 2005, pp. 313–317.

[19] A. Anzalchi, M. Moghaddami, A. Moghaddasi, M. M. Pour, and A. Sarwat, "A modified higher order power filter for grid-connected renewable energy systems," in *2016 IEEE/IAS 52nd Industrial and Commercial Power Systems Technical Conference (I&CPS)*, May 2016, pp. 1–9.

[20] M. Liserre, F. Blaabjerg, and S. Hansen, "Design and control of an lcl-filter based three-phase active rectifier," in *Industry Applications Conference, 2001. Thirty-Sixth IAS Annual Meeting. Conference Record of the 2001 IEEE*, vol. 1, Sept 2001, pp. 299–307 vol.1.

[21] M. Huang, F. Blaabjerg, P. C. Loh, and W. Wu, "Stability analysis and active damping for llcl-filter based grid-connected inverters," in *Power Electronics Conference (IPEC-Hiroshima 2014 - ECCE-ASIA), 2014 International*, May 2014, pp. 2610–2617.

[22] J. Bloemink and T. Green, "Reducing passive filter sizes with tuned traps for distribution level power electronics," in *Power Electronics and Applications (EPE 2011), Proceedings of the 2011-14th European Conference on*, Aug 2011, pp. 1–9.

[23] S. Sridharan and P. T. Krein, in *2015 IEEE International Electric Machines Drives Conference (IEMDC)*.

[24] K. Hatua, A. K. Jain, D. Banerjee, and V. T. Ranganathan, "Active damping of output filter resonance for vector-controlled vsi-fed ac motor drives," *IEEE Transactions on Industrial Electronics*, vol. 59, no. 1, pp. 334–342, 2012.

[25] A. A. Rockhill, M. Liserre, R. Teodorescu, and P. Rodriguez, "Grid-filter design for a multimegawatt medium-voltage voltage-source inverter," *IEEE Transactions on Industrial Electronics*, vol. 58, no. 4, pp. 1205–1217, April 2011.

[26] M. Davari and Y. A. R. I. Mohamed, "Dynamics and robust control of a grid-connected vsc in multiterminal dc grids considering the instantaneous power of dc- and ac-side filters and dc grid uncertainty," *IEEE Transactions on Power Electronics*, vol. 31, no. 3, pp. 1942–1958, March 2016.

[27] Masoud Davari, "Dynamics, Robust Control, and Power Management of Voltage-Source Converters in Hybrid Multiterminal AC/DC Grids," Ph.D. dissertation, University of Alberta, Edmonton, Jan. 2016. [Online]. Available: https://era.library.ualberta.ca

[28] M. Davari and Y. A. R. I. Mohamed, "Variable-structure-based nonlinear control for the master vsc in dc-energy-pool multiterminal grids," *IEEE Transactions on Power Electronics*, vol. 29, no. 11, pp. 6196–6213, Nov 2014.

Arash Anzalchi (S'14) received his B.S. and M.S. degrees in Electrical Engineering from the K.N. Toosi University of Technology and Science and Research Branch, I.A.U Tehran, Iran in 2007 and 2011 respectively.

He is currently working as a Graduate Assistant pursuing his Ph.D. at Florida International University, Miami, FL, USA. He is also one of the researchers of the "Energy Power Reliability and Analytic Center (EPRAC)", which conducts high-end studies on the effect of high penetration PV integration into the Distribution Grid. His research interests include Photovoltaic integration into the distribution grid, mitigation of power quality issues and smart power electronic technologies for the renewable energy sources.

Masood Moghaddami (S'15) received the B.S. degree from Amirkabir University of Technology, Tehran, Iran, in 2009, the M.S. degree from Iran University of Science and Technology, Tehran, Iran, in 2012.

He is currently working toward the Ph.D. degree in the Department of Electrical and Computer Engineering, Florida International University, Miami, Florida. From 2011 to 2014, he worked in the industry as an engineer to design optimization of large power transformers. His research interests include finite element analysis, power electronics, contactless power transfer, and renewable energy systems.

Amir Moghadasi (S'11)(M'16) received the B.Sc. degree in electrical engineering from Shaded University, Tehran, Iran, in 2007, the M.Sc. degree in electrical engineering from Iran University of Science and Technology (IUST), Tehran, in 2009, and the PhD. Degree in electrical engineering from Florida International University, Miami, FL, USA, in 2016.

Dr. Moghadasi is currently working as a Post-doctoral research associate at Florida International University. He is the lead researcher at FPL-FIU Solar Research Center to lead a research study on analysis of the effects of real-time operating the 1.4 MW PV systems installed at the FIU on the Florida, Power and Light (FPL) distribution circuit. His research interests are power electronics, design and control of power converters, high-penetration renewable systems, power quality, and application of computational intelligence techniques in power systems.

Maneli Malek Pour (S'15) received her Bachelor?s degree in Computer Science from Shahid Beheshti University, Tehran, Iran. She is currently working as a Graduate Research Assistant, pursuing her M.S degree in Department of Electrical and Computer Engineering, Florida International University under the supervision of Dr. Arif Sarwat. Her current research includes reliability analysis of Advanced Metering infrastructure meters(Temperature/Humidity), and life expectancy and accelerated aging of Smart Grid products and components. She is also interested in Machine Learning and Data Mining Algorithms and techniques.

Arif I. Sarwat (M'08-SM'16) received the M.S. degree in electrical and computer engineering from the University of Florida, Gainesville, FL, USA, in 2005, and the Ph.D. degree in electrical engineering from the University of South Florida, Tampa, FL, in 2010.

He worked in industry (SIEMENS) for nine years, executing many critical projects. Before joining Florida International University, Miami, FL, USA, as an Assistant Professor, he was an Assistant Professor of electrical engineering at the University at Buffalo,State University of New York, Buffalo, NY, USA. His significant work in energy storage, microgrid, and DSM is demonstrated by Sustainable Electric Energy Delivery Systems in Florida. His research interests include smart grids, high-penetration renewable systems, power system reliability, large-scale distributed generation integration, large-scale data analysis, cyber security, and vehicular technology.